EXPERIMENTAL AND NUMERICAL STUDY OF COOLING AIR FLOW IN A HYDROELECTRIC GENERATOR

***P. Moradnia*[1], *V. Chernoray*[1] *and H. Nilsson*[1]**

[1] ***Chalmers University of Technology, Gothenburg-Sweden***
pirooz.moradnia@chalmers.se

2012.06.06

Abstract

The cooling air flow inside an electric generator has been numerically simulated and validated with experimental measurements. The numerical studies are performed using OpenFOAM in a quasi-steady mode at three rotor speeds. The numerical and experimental results show similar flow distributions.

1 Introduction

Convective cooling of hydroelectric generators is an important issue, not only in increasing the efficiency of the power plants, but also in reducing the maintenance requirements of certain machine components [1]. The flow of the cooling air is complicated and geometry-dependent. The current study is aimed towards a better understanding of the flow, which is essential in modeling the convective heat transfer in these machines. In previous work [2, 3] the cooling air flow in generators with different rotor and stator geometries has been numerically investigated and conclusions regarding the effect of different geometrical modifications on the flow have been drawn. In another study [4] the numerically simulated flow at the inlet and the outlet of a generator was compared to experimental measurements. Toussaint et. al. [5] presents different numerical strategies, depending on the rotational speeds of the rotor and the nature of the flow.

The present work gives a deeper analysis of the flow characteristics as well as the influence of different rotor speeds. The experimental measurements have been conducted on a test rig, while the numerical simulations were performed on a number of cases based on the experimental facilities.

2 Cases and properties

The generator used in this work is axially cooled, i.e. the cooling air flow is axial in the rotor-stator air gap. Figure 1 shows the experimental rig during installation, the generator geometry used in the computations, and a close-up view of the stator cooling channels. The rotor consists of 12 electromagnetic poles and 12 radial fan blades above the poles. The stator is comprised of 4 cooling channel rows in the axial direction, each row including 108 cooling channels in the tangential direction, each embracing an electric coil. A casing with 12 openings in the tangential direction (here referred to as casing windows) embraces the stator. The casing connects the stator to the holding frame. The stator has a horizontal baffle on top in order to confine the inlet. A horizontal baffle is installed at the bottom of the stator, so that the air can only flow into the machine from above. A vertical baffle has also been mounted above the stator in the experimental facility, which is included in the computational domain.

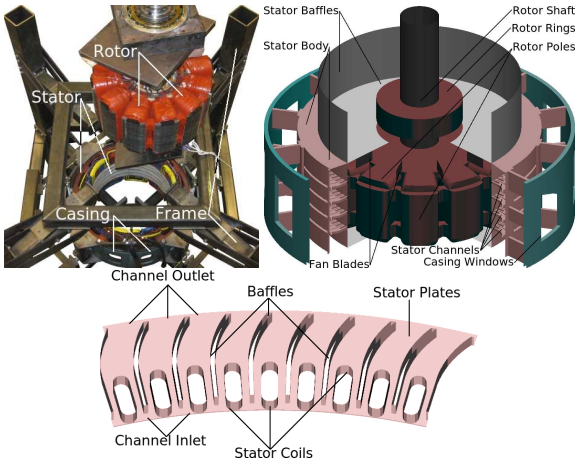

Figure 1: Top left: The experimental rig during installation. Top right: The geometry used in the simulations. Bottom: The stator cooling channels.

Since the number of stator cooling channels and coils (108) is divisible by the number of rotor poles, fan blades and casing windows (12), the computational domain can be reduced to a $1/12$ sector in the tangential direction, including 9 cooling channels in each channel row, one rotor pole and one casing window, while employing cyclic boundary conditions at the sides of the domain. The computational domain is generated without inlets and outlets, so that the volume flow through the generator is determined by the solution, rather than by an imposed value at the inlet. Figure 2 shows the computational domain, and the stator channel numbering.

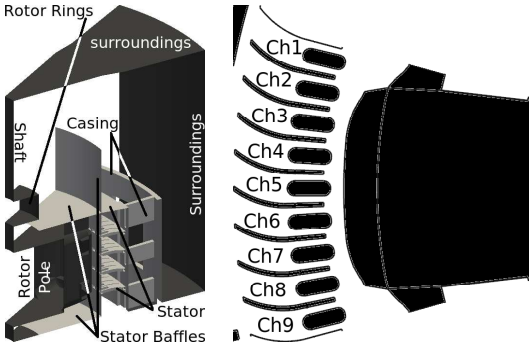

Figure 2: Left: The computational domain. Right: Stator channel numbering, top view.

Case name	$\Omega[rpm]$	Rotation direction
CW_{250}	250	Clockwise
CW_{500}	500	Clockwise
CW_{1000}	1000	Clockwise
CCW_{500}	500	Counter-Clockwise

Table 1: The numerical cases and their properties.

Four cases have been investigated numerically with different rotor speeds and rotation directions. Table 1 summarizes the properties of all numerical cases. Case CW_{500} has the same rotational speed and rotation direction as in the experiments and is hence the reference case. The modifications in the rotor speed includes clockwise rotation (CW) at 250 and $1000[rpm]$ as well as counterclockwise rotation (CCW) at $500[rpm]$, when seen from above.

3 Mathematical modeling

The air flow in the generator is complex and the velocities involved are in the turbulent regime. Hence, a suitable set of mathematical equations and discretization methods should be chosen to predict the flow. The steady-state Reynolds-Averaged Navier-Stokes equations are solved using the finite volume method and the Frozen Rotor approach. A block-structured mesh is generated by the OpenFOAM blockMesh mesh generator, and $m4$ parametrization. The mesh consists of about $17M$ cells with wall y^+ values around 5, requiring a low-Re turbulence model.

The steady-state Frozen Rotor approach is based on a multiple reference frame method. In this method an inertial and a rotating region are specified, separated from each other by an axi-symmetric interface [6]. The rotating region is provided with extra source terms to account for the rotation. The Navier-Stokes and continuity equations in the inertial region read

$$\nabla \cdot (\vec{u}_I \otimes \vec{u}_I) = -\nabla(p/\rho) + \nu\nabla^2\vec{u}_I \qquad (1)$$
$$\nabla \cdot \vec{u}_I = 0$$

where $\vec{u}_I$ is the velocity in the inertial reference frame. The Navier-Stokes and continuity equations based on the convection of the absolute velocity $\vec{u}_I$ in the rotating part of the domain is then given by

$$\nabla \cdot (\vec{u}_R \otimes \vec{u}_I) + \vec{\Omega} \times \vec{u}_I = -\nabla(p/\rho) + \nu\nabla^2\vec{u}_I \quad (2)$$
$$\nabla \cdot \vec{u}_I = 0$$

where $\vec{u}_R$ is the velocity in the rotating frame of reference and $\vec{\Omega}$ is the rotation vector of the rotating frame of reference. The use of the Frozen Rotor approach gives a reasonable solution of the average flow in the generator, despite its general dependence on the rotor-stator interface location and pole-channel relative position [7]. In the present generator, the channel inlets are much smaller than the pole width, meaning that the relative position of the pole and channels will have a weaker effect on the flow inside the channels. However, the relative positioning of the pole and the outer casing should be taken into account when interpreting the results.

The turbulence is modeled employing the low-Re Launder-Sharma $k-\varepsilon$ model, demanding that the computational mesh should consists of very fine cells, especially in the near wall regions, where the y^+ values should not exceed 10. The transport equations for the turbulent quantities read [8]

$$\frac{Dk}{Dt} = \qquad (3)$$
$$\left[\left(\nu + \frac{\nu_t}{\sigma_k}\right)k_{,j}\right]_{,j} + \nu_t\left(u_{i,j} + u_{j,i}\right)u_{i,j} - \varepsilon$$

$$\frac{D\tilde{\varepsilon}}{Dt} = \left[\left(\nu + \frac{\nu_t}{\sigma_\varepsilon}\right)\tilde{\varepsilon}_{,j}\right]_{,j} \qquad (4)$$
$$+c_{1\varepsilon}f_1\nu_t\frac{\tilde{\varepsilon}}{k}\left(u_{i,j} + u_{j,i}\right)u_{i,j} - c_{2\varepsilon}f_2\frac{\tilde{\varepsilon}^2}{k} + E$$

where the parameters are shown in Table 2

ν_t	ε	D	E
$C_\mu f_\mu \frac{k^2}{\tilde{\varepsilon}}$	$\tilde{\varepsilon} + D$	$2\nu\left(\frac{\partial\sqrt{k}}{\partial x_j}\right)^2$	$2\nu\nu_t\left(\frac{\partial^2 u_i}{\partial x_j^2}\right)^2$
R_T	f_1	f_2	f_μ
$\frac{k^2}{\nu\tilde{\varepsilon}}$	1	$1 - 0.3e^{-R_T^2}$	$e^{\frac{-3.4}{(1+R_T/50)^2}}$

Table 2: The parameters for the Launder-Sharma $k-\varepsilon$ turbulence model.

It should be noticed that $X_{i,j} \equiv \frac{\partial X_i}{\partial x_j}$, and that k and $\tilde{\varepsilon}$ should be set to zero at the walls. The numerical convergence procedure reveals a tendency for unsteady behavior. The convergence is thus assessed by the requirements of well-stabilized residuals, rotor torque, and total volume flow in the machine, as well as minimal fluctuations in the velocity field.

4 Experimental setup

The experimental rig is a small-scale generator located at Uppsala University in Uppsala city, Sweden,

see Figure 1. The rotor radius is $0.356m$, and the stator inner radius is $0.365m$. The stator cooling channels have a height of $9.4mm$.

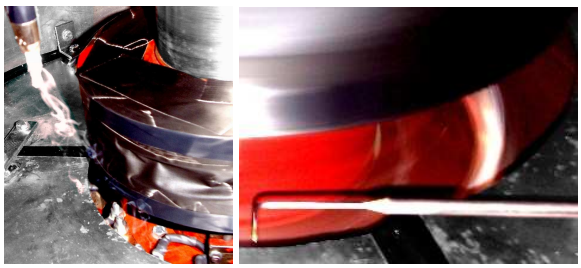

Figure 3: Left: Smoke visualization of the flow at the inlet. Right: The 5-hole probe used in measuring the velocities at the inlet.

The experiments consist of flow visualizations as well as flow measurements at the inlet and the outlet of the generator. The flow visualizations were performed by smoke pens, as shown in Figure 3. The smoke pens were placed at different axial, radial and tangential positions at the inlet of the generator to monitor the flow streamlines. The flow visualizations demonstrated that the inlet flow was turbulent and axi-symmetric.

The flow measurements at the inlet were performed using a five-hole pressure probe, shown in Figure 3. The probe is of L-type with a tip diameter of $1.6mm$. The probe was calibrated for the cone angles from 0 to $52°$. To spatially position the probe at the generator inlet, a two-axial traversing system was used. The traversing system movement is controlled by stepper motors with a resolution of better than $2\mu m$. A dedicated PC was used to control the motion of the traversing system. The precision of the measurements by the 5-hole probe is predominantly defined by the initial positioning of the probe in the facility. The tolerance of the initial positioning of the probe was $0.1mm$ in the axial direction, $1mm$ in the radial direction and $1°$ in the angular direction.

The outlet flow measurements were performed using a total pressure probe rake, see Figure 4. The rake is comprised of 15 total pressure tubes mounted in a holder. The rake holder is designed to position the rake precisely along the channel center plane at the outlet.

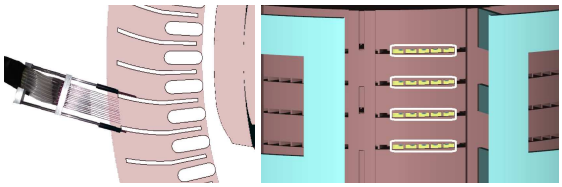

Figure 4: Left: The position of the total pressure rake in the channels. Right: The accessible channels in an open casing window, viewed from outside.

Figure 4 shows the position of the total pressure rake in the channels. The rake tubes are positioned along the flow to maintain the best accuracy of the total pressure measurements (the incoming flow angle within $10°$). Figure 4 also shows the accessible channels in an open casing window viewed from outside the stator. The corresponding casing is removed in the figure for better visibility. As can be seen, only 5 out of 9 channels in each row were available for measurements in each open window (channels 4 to 8 in Figure 2). In one open window, two extra channels were blocked by electric cables. The mountings of the holding frame, as well as a number of electric cables and equipment partly block 5 casing windows (out of 12). This means that some additional flow blockage occurs in the experimental rig, compared to the the numerical cases. Nevertheless, as Figure 1 shows, the windows are not completely blocked, as the casing is open from the top and bottom. This results in 138 accessible channels out of 432. The velocity magnitude at the outlet is computed from the total pressure as:

$$|U| = \sqrt{2(p_{tot} - p_{stat})/\rho} \tag{5}$$

The static pressure was assumed to be constant and equal to the ambient pressure in the laboratory. The pressures from the five-hole probe and the total pressure rake were monitored using a 16-channel $PSI9116$ digital pressure scanner (Pressure Systems Inc.). The measuring range of the scanner transducers is $\pm 2500[Pa]$ and the channel scanning frequency is $500[Hz]$. To maintain the highest possible accuracy in a low-pressure range the pressure transducers were regularly controlled for an offset and nulled before each set of measurements. The resulting precision of the transducer offset was better than $0.2[Pa]$ which is also defining the measurement accuracy. The time-mean statistics were evaluated from 1000 samples for each channel in the case of the total pressure rake, and from 2000 samples per channel in the case of the five-hole probe. Thus, under the acquisition time intervals, the rotor was rotating 16 or 33 revolutions, respectively.

5 Results

The flow parameters mainly investigated in the numerical simulations include volume flow, velocity distributions inside the machine, and inlet and outlet velocity distributions.

5.1 Flow pattern at the inlet

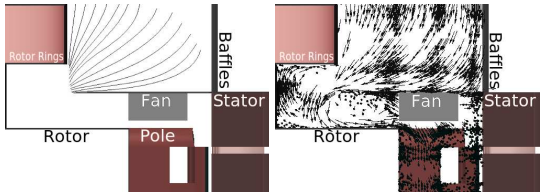

Figure 5: Left: A schematic view of the smoke-visualized flow pattern at the inlet. Right: The computed unit vectors of the velocity at the inlet.

Figure 5 shows a schematic view of the smoke-visualized flow pattern at the inlet, and the unit vectors of the computed velocity at the inlet to the machine. A comparison suggests that the experimental measurements confirm the numerical results. Just above the stator horizontal baffle the flow is purely radial. The radial component vanishes gradually, while an axial component grows as the observer moves closer to the rotor rings. At the rotor rings the flow does not have any radial component. The numerical results show a separation zone just under the stator horizontal baffle at the inlet, caused by the sudden change of the flow direction as the fluid enters the machine. The flow pattern is similar for all numerical cases.

5.2 Inlet velocity profiles

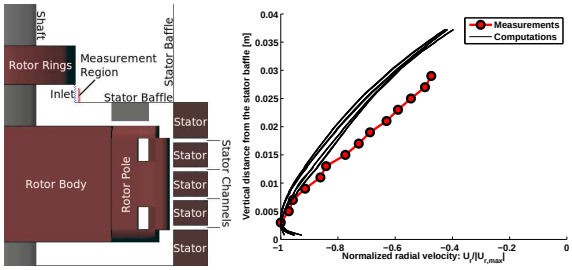

Figure 6: Left: Cross-section view of the generator geometry with the location of the inlet measurement. Right: The computed and measured normalized radial velocity at the inlet to the generator.

Figure 6 shows a cross-sectional view of the generator with the location of the inlet measurement, visualized by a dashed line. The 5-hole probe was positioned along the inlet, with the probe head $19mm$ radially outside the rotor rings. Due to the restriction of maximum probe measuring angle ($52°$), the inlet flow was considered resolved for the interval $0 - 29mm$ from the horizontal stator baffle. Figure 6 shows the normalized radial velocities at the inlet obtained by measurements and computations. The curves are normalized by the maximum value of each case, since the flow rate differs for each case. The black curves show the numerical results for the four computational cases along 5 different tangential positions for each case. The radial velocity is thus axi-symmetric and have similar behaviors in all numerical cases. The behavior of the computed and measured profiles are similar. The radial velocity develops quickly to the maximum (negative) value near the stator baffle, decreasing smoothly to about 40% of the maximum value near the rotor rings.

5.3 Velocity components just above the rotor pole

Figure 7 shows the velocity contours of CW_{500} just above the pole, normalized by the average axial velocity at the same plane. The distributions are similar for all computational cases. The pole boundaries are shown for a better understanding. For the normalized axial velocity, a negative axial velocity indicates an inward flow into the machine (desirable). The largest inward axial velocities (darker colors) are observed between the poles and closer to the trailing edge, where the static pressure is lowest (see Figure 8). At the leading edge there are only upward axial velocities (bright colors) as the flow is deflected upwards when meeting the pole from below the fan blades. Just above the pole surface the axial velocity is zero. The axial velocity tends to be more inwards closer to the stator inner wall, caused by the higher pressure, forcing the flow through the machine.

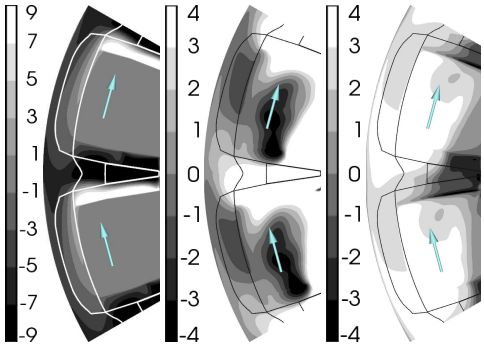

Figure 7: Velocity contours of CW_{500} just above the pole, normalized by the average axial velocity at the same level. Left: Axial component, $\frac{U_a}{U_a}$. Middle: Radial component, $\frac{U_r}{U_a}$. Right: Tangential component, $\frac{U_t}{U_a}$.

For the normalized radial velocity, positive values indicate a radial velocity towards the stator (desirable). The largest outward radial velocities (bright colors) are observed near the shaft and between the poles. As the flow moves radially outward the radial velocity decreases due to the area change. Close to the stator the radial velocities stay mostly positive and are relatively weak as the presence of the stator wall is felt. The negative regions just above the pole (darker colors) indicate recirculation.

For the normalized tangential velocity, positive values refer to the direction of the pole rotation (desirable). The largest positive tangential velocities (bright colors) are observed on top of the pole and close to the trailing edge of the pole in the air gap. Negative values appear between the poles and close to the shaft, where recirculation occurs.

5.4 Pressure distribution on the rotor poles

Figure 8 shows the static pressure contours normalized by the total pressure on the pole surfaces for case CW_{500}. The contours are similar for all computational cases. The regions close to the rotor shaft show low and negative values for the static pressure, bringing about a suction effect and drawing the air into the machine. On the top and close to the trailing edge the static pressure is high. Also, on top of the pressure side, a region of high static pressure is observed. These observations are justified by noticing

Figure 8: The relative pressure normalized by the total pressure on the rotor pole surfaces. Left: Suction surface. Middle: top surface. Right: Pressure surface.

that between the poles and just above the trapezoidal pole supports there is a fan blade which only leaves room for fluid flow from below. The fluid accelerates and meets the leading edge of the pole, increasing the static pressure (stagnation pressure). The flow separates just after the leading edge and gets forced down by the next fan blade while moving along the pole.

5.5 Flow in the stator channels

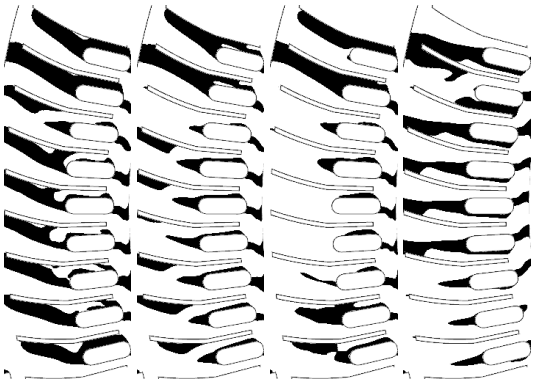

Figure 9: Recirculation zones (black) in the top row stator channels. Left to right: CW_{250}, CW_{500}, CW_{1000} and CCW_{500}

Figure 9 shows the flow pattern in the top row stator channels. The black regions indicate recirculation zones. Flow separation and recirculation occur on the downstream side of the coils, as well as on one of their sides. The recirculation zones become smaller with increasing rotational speed of the rotor. Case CCW_{500} demonstrates approximately the same total size of the recirculation zones as Case CW_{500} but the recirculation zones have moved to new locations. This is caused by the different channel curvatures relative to the rotation direction of the pole. The channels which experience a blockage near the outlet (channels $Ch1$ and $Ch2$ in Figure 2) have larger recirculations than the rest of the channels. This may also be dependent on the position of the pole.

5.6 Velocity profiles at the outlet

Figure 10 shows the computed (CW_{500}) and the measured velocity magnitudes at the outlet of the stator channels. The measured data are extracted at the channels highlighted in Figure 4. The vertical lines

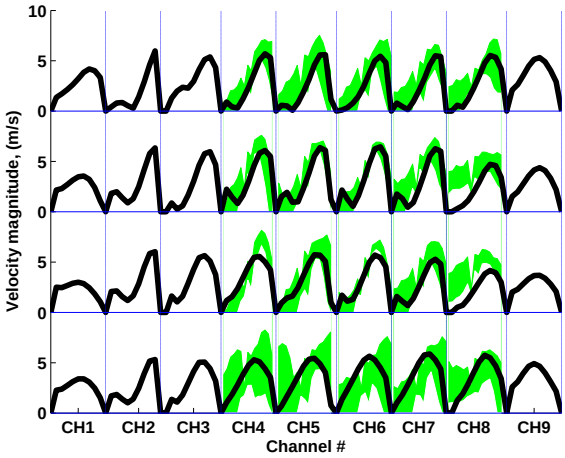

Figure 10: Computed and measured velocity magnitudes at the outlet of the stator channels.

show the stator channel sides, while the horizontal lines represent the zero velocity levels at the centerline of the channel rows. The black curves show the computed results, while the shaded areas show the range of the scattered measured velocities for all available channels. The scattering of the experimental data points out that the velocities for the same channels in different casing windows vary, which can be interpreted as a non-periodicity at the outlet of the stator, imposed by the geometry. The general behavior as well as the magnitudes of the numerical profiles are very similar to the measured profiles.

5.7 Total volume flow

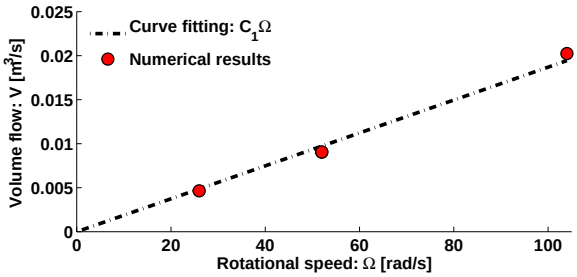

Figure 11: The total volume flow vs. rotor rotational speed in the computational cases.

Figure 11 shows the volume flow variations with the rotational speed in the simulations. The volume flow through the machine increases almost linearly with the rotational speed of the rotor, Ω, as $V = C_1\Omega$, where $C_1 \approx 1.9 \times 10^{-4} m^3$. The rotation direction of the rotor does not affect the volume flow in this case. The small non-linearity of the results depends on the losses and the flow separations which, according to Figure 9, get smaller by increasing the rotational speed.

5.8 Rotor axial power

Figure 12 shows the axial power required to rotate the rotor against the rotor rotational speed for the com-

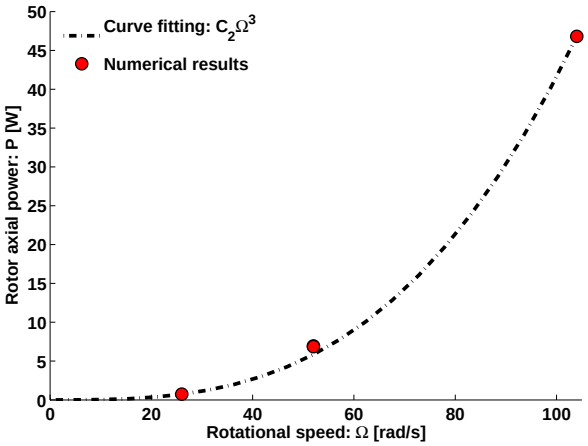

Figure 12: Rotor axial power vs. rotor rotational speed in the computational cases.

putational cases. The curve fitting data suggests that the axial power increases cubically with the rotational speed of the rotor, Ω (and hence the volume flow, V), as $P = C_2\Omega^3$, where $C_2 \approx 4.2 \times 10^{-5}[J]$. Again, the rotation direction of the rotor does not affect the required rotor power.

6 Conclusions

An important step in modeling the convective heat transfer in generators is to understand the complicated flow and the effect of the different geometrical features on the flow. The air flow in a generator has been experimentally measured and numerically simulated. The agreement between the numerical and experimental results is very promising, both qualitatively and quantitatively. The effect of different rotor speeds on the flow field has been investigated numerically and in more details. The volume flow varies almost linearly with the rotor speed, while the rotor power varies with the rotor speed cubic. The normalized pressure and velocity contours for the numerical cases at different speeds are similar and show common patterns. The flow separations in the stator reduces with increasing rotor speed.

Acknowledgments

The research presented was carried out as a part of "Swedish Hydropower Centre - SVC". SVC has been established by the Swedish Energy Agency, Elforsk and Svenska Kraftnät together with Luleå University of Technology, The Royal Institute of Technology, Chalmers University of Technology and Uppsala University. www.svc.nu

The computational time, hardware and facilities were provided by c^3se, center for scientific and technical computing at Chalmers University of Technology in Gothenburg Sweden and $SNIC$, Swedish National Infrastructure for Computing.

References

1Moradnia, P. (2010), CFD of air flow in hydro power generators, Thesis for licentiate of engineering no. 2010:11, ISSN 1652- 8565, Chalmers University of Technology, Sweden.

2Moradnia, P., and Nilsson, H. (2010), CFD of air flow in hydro power generators for convective cooling, using OpenFOAM, ECCOMAS CFD 2010 Paper 556.

3Moradnia, P. and Nilsson, H. (2011), A parametric study of the air flow in an electric generator through stepwise geometry modifications. An ECCOMAS Thematic Conference, CFD and OPTIMIZATION Paper 040.

4Moradnia, P., Chernoray, V. and Nilsson, H. (2011), Experimental and numerical investigation of the cooling air flow in an electric generator, HEFAT 2011 International Conference on Heat Transfer, Fluid Mechanics and Thermodynamics, pp. 242-249.

5Toussaint, K., Torriano, F., Morissette, J.F., Hudon, C., and Reggio, M. (2011), CFD analysis of ventilation flow for a scale model hydrogenerator, ASME Power Paper 55202

6Petit, O., Page, M., Beaudoin, M., and Nilsson, H. (2009), The ERCOFTAC centrifugal pump OpenFOAM case study, IAHR International meeting of the workgroup on cavitation and dynamic problems in hydraulic machinery and systems, pp. 523-532.

7Houde, S., Hudon, C., and Vincent, P.B. (2008), Simulation strategies of the cooling flow for large hydro-generators, *Hydropower & Dams*, Issue 6.

8Launder B.E. and Sharma B.I. (1974), Application of the energy dissipation model of turbulence to the calculation of flow near a spinning disc, *Lett.* Heat Mass Transfer, Paper 1 1318.